ADVANCED FUNCTIONAL MATERIALS

Supporting Information

for *Adv. Funct. Mater.,* DOI: 10.1002/adfm.202113030

$CaV_6O_{16}\cdot 2.8H_2O$ with Ca^{2+} Pillar and Water Lubrication as a High-Rate and Long-Life Cathode Material for Ca-Ion Batteries

Junjun Wang, Jianxiang Wang, Yalong Jiang, Fangyu Xiong, Shuangshuang Tan, Fan Qiao, Jinghui Chen, Qinyou An, and Liqiang Mai**

Supporting Information

$CaV_6O_{16}·2.8H_2O$ with Ca^{2+} pillar and water lubrication as a high-rate and long-life cathode material for Ca-ion batteries

Junjun Wang, Jianxiang Wang, Yalong Jiang, Fangyu Xiong, Shuangshuang Tan, Fan Qiao, Jinghui Chen, Qinyou An, Liqiang Mai**

Experimental section

Materials synthesis. $CaV_6O_{16}·2.8H_2O$ nanobelt was synthesized by one-step hydrothermal method. Firstly, 4 mmol V_2O_5 and 2 mmol $Ca(OH)_2$ were added to 80 mL ultra-pure water and then the above solution was stirred at 70 °C for 3 h. Afterwards, the obtained solution was transferred into a 100 mL Teflon-lined stainless steel autoclave. The sealed autoclave was put into an oven at 180 °C for 24 h. Finally, the dark red product was centrifuged and washed with deionized water for three times and absolute ethanol for three times, respectively. The obtained dark red product was dried in a vacuum drying oven at 60 °C for 12 hours.

Material characterization. *In situ* XRD measurement was performed using a Bruker AXS D8 Advance powder X-ray diffractometer with an area detector using Cu Kα X-ray source. *Ex situ* and powder XRD measurement was performed using a Bruker AXS D2 Advance powder X-ray diffractometer with a detector using Cu Kα X-ray source. Scanning electron microscope (SEM) images were acquired by using a JEOL-7100F microscope. A Titan G2 60-300 instrument was used for transmission electron microscopy (TEM), high resolution TEM, high-angle annular dark field (HAADF) images and energy dispersive X-ray spectroscopy (EDX) maps tests. VG Multi Lab 2000 instrument was used for XPS

measurement. Thermogravimetric analysis (TGA) was carried out on a NETZSCH-STA449F5 thermo-analyzer with a heating rate of 10 ˚C min^{-1} and air atmosphere. Fourier Transform Infrared Spectroscopy (FTIR) transmittance spectra and *in situ* FTIR were carried out by a Nicolet 6700 (Thermo Fisher Scientific Co., USA) IR spectrometer.

Electrochemical tests. The positive electrode consisting of $CaV_6O_{16}·2.8H_2O$ (70 wt%), acetylene black (AB, 20 wt%), and poly(vinylidene fluoride (PVDF, 10 wt%). They were mixed and dispersed in N-methyl-2-pyrrolidinone (NMP) to form a slurry, and the slurry was cast onto Al foil and dried at 70 °C for 24 h. Finally, the Ca^{2+} storage performances of CVO was tested by CR2016 coin cell assembled with the prepared positive electrode, GF/A as separator, 0.3 M $Ca(TFSI)_2$ in ethylene glycol dimethyl ether (DME) or diethylene glycol dimethyl ether (G2) as the electrolyte and ACC (1500-2500 m^2 g^{-1}, GUN EI Chemical Industry Co. Ltd.) as both reference and counter electrode. The loading of active materials on the cathode (10 mm diameter) is about 1.0 mg cm^{-2} and the loading of ACC (12 mm diameter) is about 16.0 mg cm^{-2}. $Ca[B(hfip)_4]_2$ was prepared according to previous related reports.[1, 2] 0.2 M $Ca[B(hfip)_4]_2$/DME electrolyte was adopted when Ca metal used as anode. The water content of ACC and electrolyte were evaluated by Karl Fisher titration. The water content of G2 solvent after the activated carbon cloth (12 mm) soaked in G2 solvent (3 ml) for 24 hours is 13.58 ppm and the water content of 0.3 M $Ca(TFSI)_2$/G2 electrolyte is 74.26 ppm. Therefore, the capacity contributed by proton intercalation should be negligible. Electrochemical performance measurement with $Ca(TFSI)_2$ based electrolyte was conducted at 50 ℃ and room temperature, and with $Ca[B(hfip)_4]_2$/DME electrolyte was conducted at room temperature. A multichannel battery testing system (LAND CT2001A) was used. Cyclic voltammetry (CV) tests were performed with an Autolab PGSTAT 302N electrochemical workstation at 50 ℃. *In situ* XRD and *in situ* FTIR tests were carried out at room temperature.

Computational details. All calculations on $CaV_6O_{16}\cdot 3H_2O$ were executed by the projector augmented wave (PAW)[3] method within density functional theory (DFT), conducted in the Vienna ab initio Simulation Package (VASP)[4, 5]. The generalized gradient approximation (GGA) in the form of the Perdew-Burke-Ernzerhof (PBE)[6] was used to treat the exchange-correlation energy. Based on reported results,[7, 8] the crystal structure of $CaV_6O_{16}\cdot 3H_2O$ is constructed and the H_2O is fixed during structural relaxation. Then, the Ca^{2+} migration pathway in $CaV_6O_{16}\cdot 3H_2O$ and energy barrier were optimized with nudged elastic band (NEB) method in a 1×2×1 supercell containing 2 formula units (4 Ca, 24 V, 76 O, and 24 H). As shown in Figure S15a, 5d, and S16a, three possible diffusion paths were considered. A kinetic energy cutoff of 500 eV was used for wave functions expanded in the plane wave basis. Besides, spin polarization was considered. Allow all atoms to relax until the forces were less than 0.05 eV $Å^{-1}$. For the Brillouin-zone sampling, 2×2×2 k-points for the supercell were adopted to ensure convergence of the total energy.

Table S1. Rietveld refinement atomic coordinates for CVO.

Atom	Site	Occupancy	x	y	z
Ca1	4i	0.25	0.4440	0	0.0073
Ca2	4i	0.25	0.1056	0.5000	0.0362
V1	4i	1.00	0.0222	0.5000	0.1953
V2	4i	1.00	0.3110	0	0.1758
V3	4i	1.00	0.3370	0.5000	0.2672
O1	4i	1.00	-0.0934	0.5000	0.0977
O2	4i	1.00	0.2500	0	0.0840
O3	4i	1.00	0.2820	0.5000	0.3080

O4	4i	1.00	-0.0660	0.5000	0.2300
O5	4i	1.00	0.6420	0	0.1510
O6	4i	1.00	0.3940	0	0.3130
O7	4i	1.00	0.0353	0	0.1810
O8	4i	1.00	0.3860	0.5000	0.1370
O9	4i	1.00	0.6410	0.5000	0.0159
O10	8j	0.25	0.0110	0.0440	0.0089

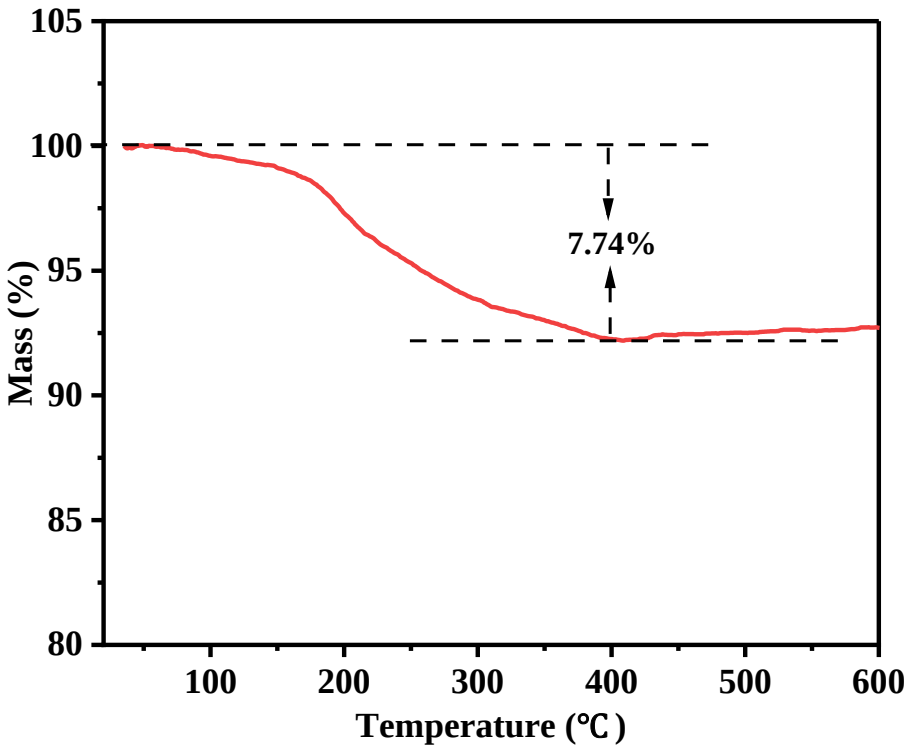

Figure S1. TGA for CVO with a heating rate of 10 ˚C min^{-1} and air atmosphere.

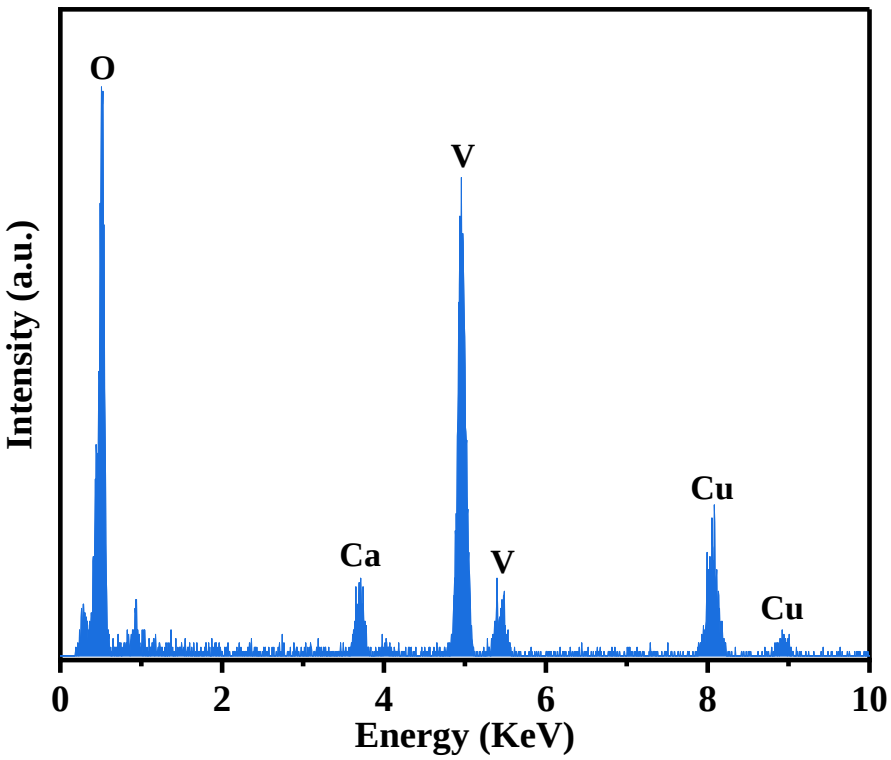

Figure S2. EDX spectrum for CVO.

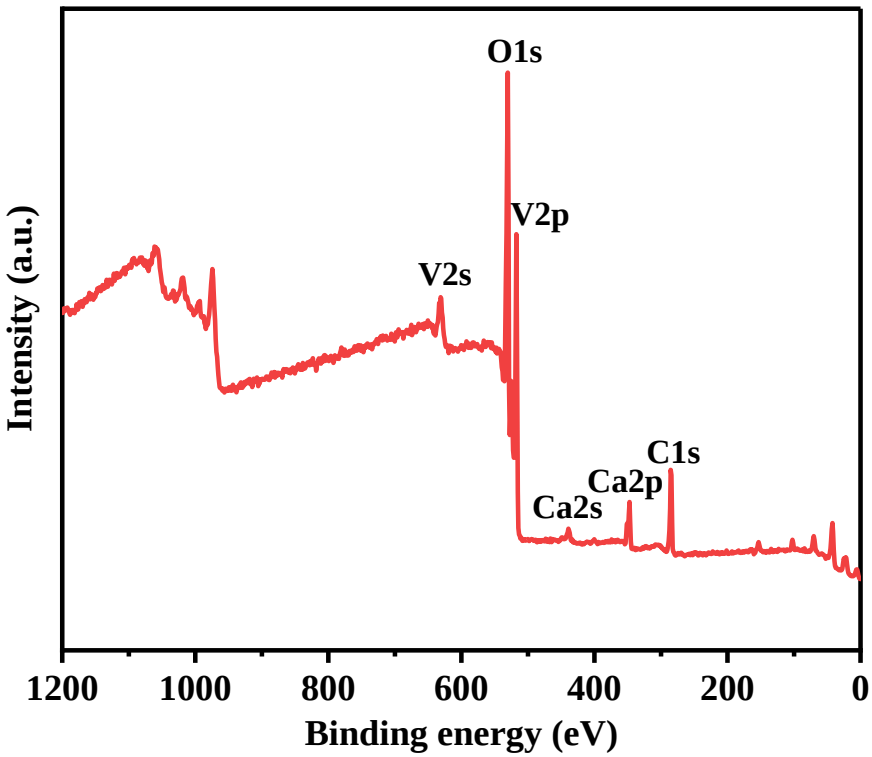

Figure S3. The wide XPS spectrum of CVO.

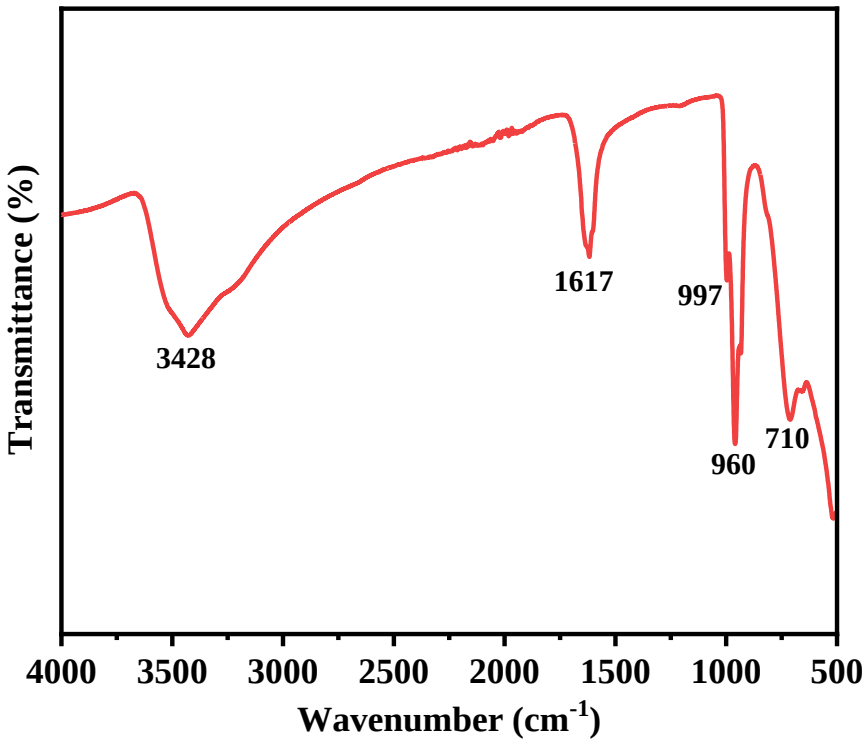

Figure S4. FT-IR spectrum of CVO.

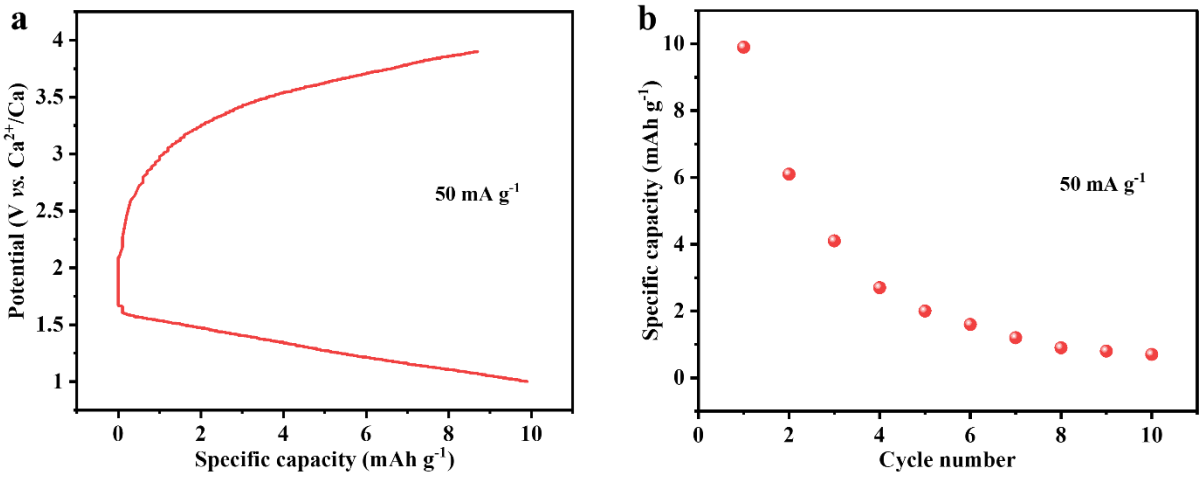

Figure S5. The charge-discharge curve (a) and cycling performance (b) of CVO with Ca metal anode and $Ca(TFSI)_2$/G2 electrolyte at 50 mA g^{-1}.

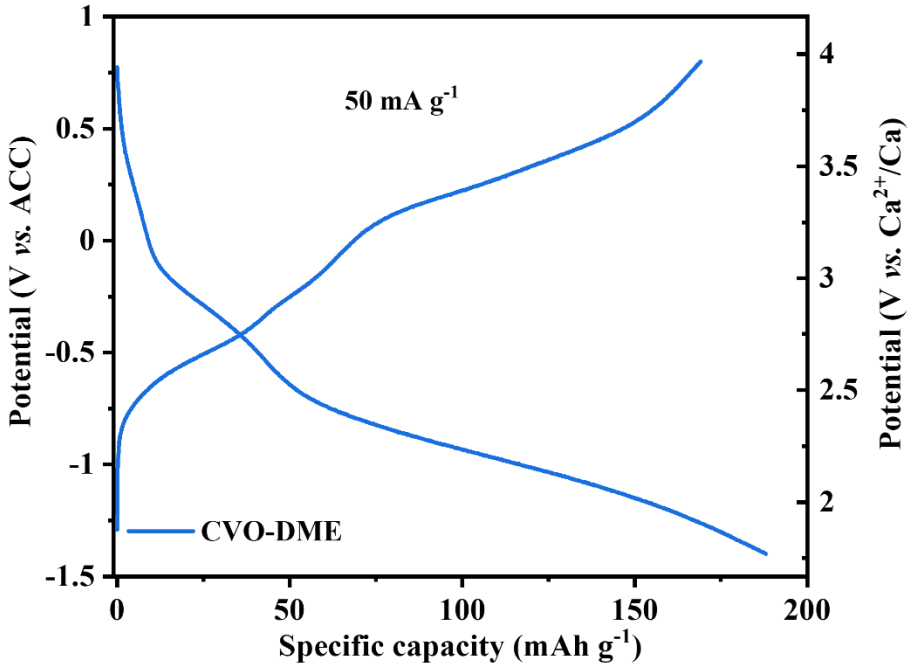

Figure S6. Galvanostatic charge/discharge profile of CVO with $Ca(TFSI)_2$/DME at 50 mA g^{-1} and 50 ℃

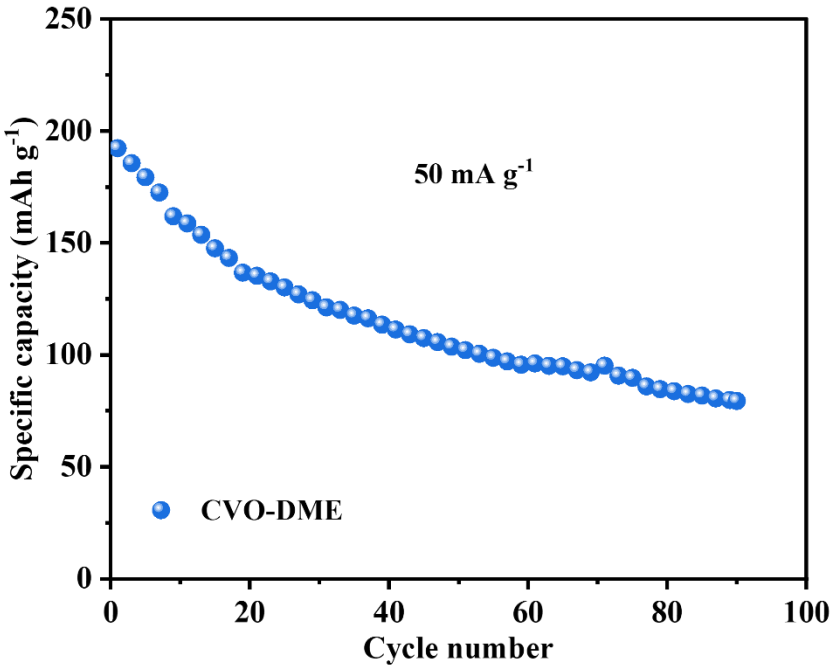

Figure S7. Cycling performances of CVO with $Ca(TFSI)_2$/DME at 50 mA g^{-1} and 50 ℃

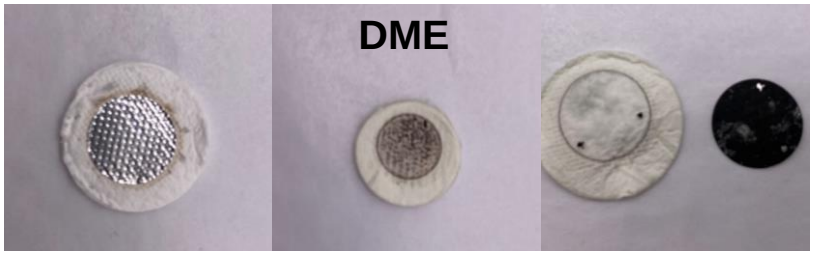

Figure S8. The photograph of disassembled coin cell with $Ca(TFSI)_2$/DME electrolyte after 50 cycles.

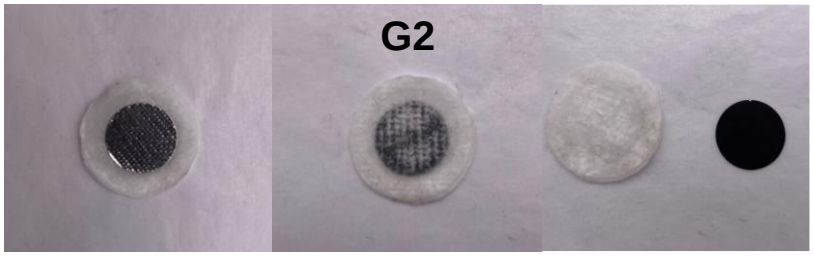

Figure S9. The photograph of disassembled coin cell with $Ca(TFSI)_2$/G2 electrolyte after 50 cycles.

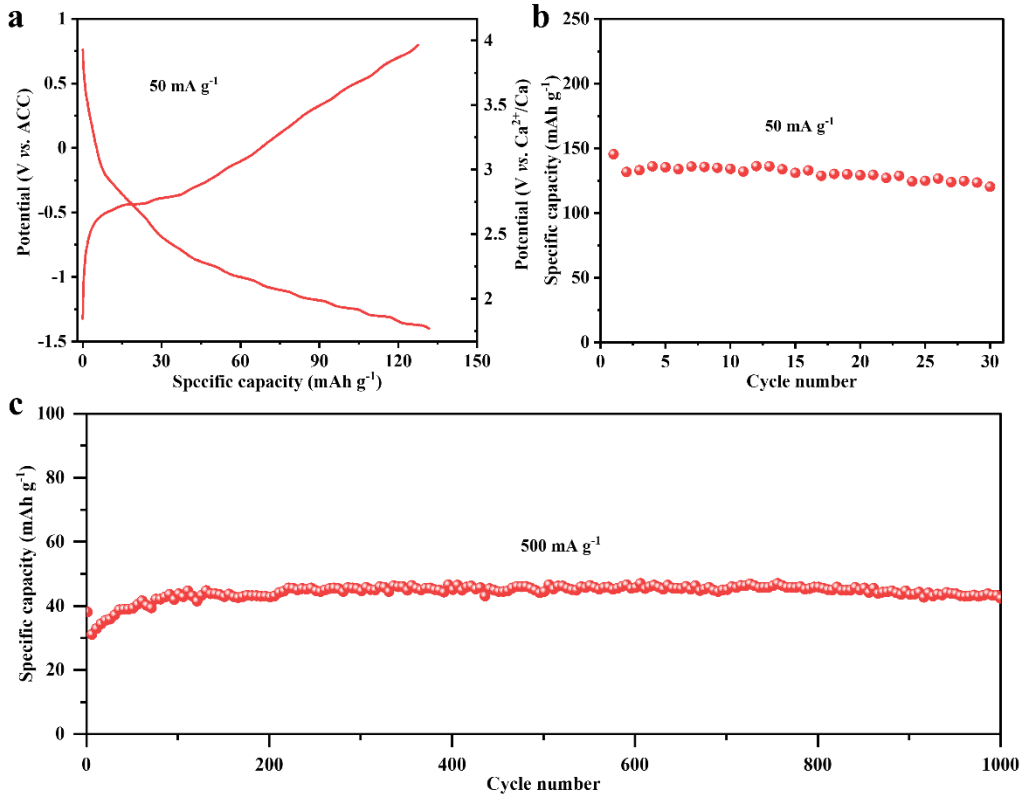

Figure S10. The Ca^{2+} storage performance of CVO with $Ca(TFSI)_2$/G2 at room temperature. (a) Galvanostatic charge/discharge profile of CVO at 50 mA g^{-1}. Cycling performances of CVO with $Ca(TFSI)_2$/G2 at (b) 50 mA g^{-1} and (c) 500 mA g^{-1}.

Table S2. The Ca^{2+} storage performance of CVO and the reported inorganic cathode materials for CIBs with organic electrolyte.

Cathode	Counter/reference electrode	Electrolyte	Working temperature	Reversible capacity/current density	Cycle number/capacity retention	Reference
$CaV_6O_{16}\cdot 2.8H_2O$	ACC/-	0.3 M $Ca(TFSI)_2$/G2	50 □	175.2 mAh g^{-1}/50 mA g^{-1}	100/74.7%	This work
				69 mAh g^{-1}/500 mA g^{-1}	1000/93%	
			Room temperature (RT)	131.7 mAh g^{-1}/50 mA g^{-1}	30/91.3%	
				44.9 mAh g^{-1}/500 mA g^{-1}	1000/94.4 %	
$Mg_{0.25}V_2O_5\cdot H_2O$	ACC/-	0.8 M $Ca(TFSI)_2$ in EC:PC:EMC:DMC	RT	70.0 mAh g^{-1}/100 mA g^{-1}	500/86.9%	9
$Na_xMnFe(CN)_6$	Ca_xSn/-	0.2 M $Ca(PF_6)_2$ in EC:PC	RT	100 mAh g^{-1}/10 mA g^{-1}	35/50%	10
$K_2BaFe(CN)_6$	Carbon paper/Ag-Ag^+	1 M $Ca(ClO_4)_2$ in ACN + 17vol% water	RT	60.0 mAh g^{-1}/12.5 mA g^{-1}	30/96.6%	11
$CaCo_2O_4$	V_2O_5/-	1 M $Ca(ClO_4)_2$ in ACN	RT	100 mAh g^{-1}/40 uA cm^{-2}	30/80%	12
Na_2FePO_4F	BP2000 carbon/-	0.2 M $Ca(PF_6)_2$ in EC:PC	RT	80 mAh g^{-1}/10 mA g^{-1}	50/75%	13
$NH_4V_4O_{10}$	Pt/Ag-Ag^+	$Ca(ClO_4)_2\cdot xH_2O$ in ACN	RT	150 mAh g^{-1}/100 mA g^{-1}	100/93.3%	14
α-MoO_3	Activated carbon/Ca	0.5 M $Ca(TFSI)_2$ in ACN	RT	140 mAh g^{-1}/2 mA g^{-1}	12/58%	15
V_2O_5	Activated carbon/Ag-Ag^+	1 M $Ca(ClO_4)_2$ in ACN	RT	150 mAh g^{-1}/50 uA cm^{-2}	5/20%	16

$Fe_4[Fe(CN)_6]_3$	Graphite rod/Ag-Ag^+	1 M $Ca(ClO_4)_2$ in ACN	RT	120 mAh g^{-1}/125 mA g^{-1}	80/83%	17
$KNiFe(CN)_6$	AC/Ag-Ag^+	0.5 M $Ca(TFSI)_2$ in ACN	RT	45 mAh g^{-1}/ 25 uA cm^{-2}	12/90%	18
VS_4	Ca/–	$Ca[B(hfip)_4]_2$ in DME	RT	315 mAh g^{-1}/100 mA g^{-1}	20/33%	19
TiS_2	Li/–	0.1 M $Ca(CF_3SO_3)_2$ in PC:DMC	RT	90 mAh g^{-1}/50 mA g^{-1}	3/91%	20
CuS	ACC/-	0.8 M $Ca(TFSI)_2$ in EC:PC:EMC:DMC	RT	200 mAh g^{-1}/100 mA g^{-1}	30/49.2%	21
$FeF_3{\cdot}0.33H_2O$@C	AC/Ag-Ag^+	0.5 M $Ca(TFSI)_2$ in EC:DMC	30 □	120 mAh g^{-1}/50 uA cm^{-2}	3/95%	22
$NaV_2(PO_4)_3$	AC/-	1 M $Ca(TFSI)_2$/ in ACN	RT	81 mAh g^{-1}/3.5 mA g^{-1}	40/97.6%	23
$Ca_{0.13}MoO_3{\cdot}(H_2O)_{0.41}$	AC/-	0.5 M $Ca(ClO_4)_2$/AN	RT	192 mAh g^{-1}/85.65 mA g^{-1}	50/72.8%	24
$VOPO_4{\cdot}2H_2O$	ACC/-	0.8 M $Ca(TFSI)_2$ in EC:PC:EMC:DMC	RT	71.8 mAh g^{-1}/100 mA g^{-1}	200/65%	25
$Na_{0.5}VPO_{4.8}F_{0.7}$	AC/-	1.0 M $Ca(PF_6)_2$ in EC/PC	RT	75 mAh g^{-1}/50 mA g^{-1}	500/90%	26
$K_{0.5}V_2O_5$	AC/-	0.5 M $Ca(ClO_4)_2$ in PC	RT	65 mAh g^{-1}/66.6 mA g^{-1}	100/92%	27
$FeV_3O_9{\cdot}1.2H_2O$	AC/-	0.5 M $Ca(ClO_4)_2$/AN	RT	96 mAh g^{-1}/200 mA g^{-1}	400/79%	28
β-$Ag_{0.33}V_2O_5$	AC/-	0.5 M $Ca(BF_4)_2$ in EC:PC	30 □	179 mAh g^{-1}/12.3 mA g^{-1}	50/47%	29
$Ti_2O(PO_4)_2(H_2O)$	AC/-	0.5 M $Ca(BF_4)_2$ in EC:PC	RT	60.8 mAh g^{-1}/50 mA g^{-1}	1500/95%	30

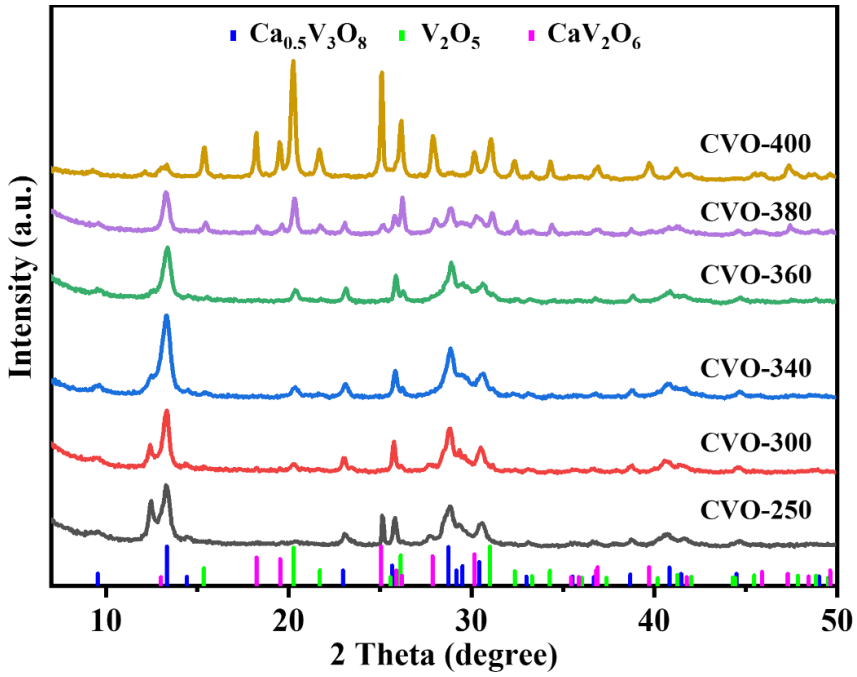

Figure S11. XRD patterns of CVO treated at different temperatures for 4 h.

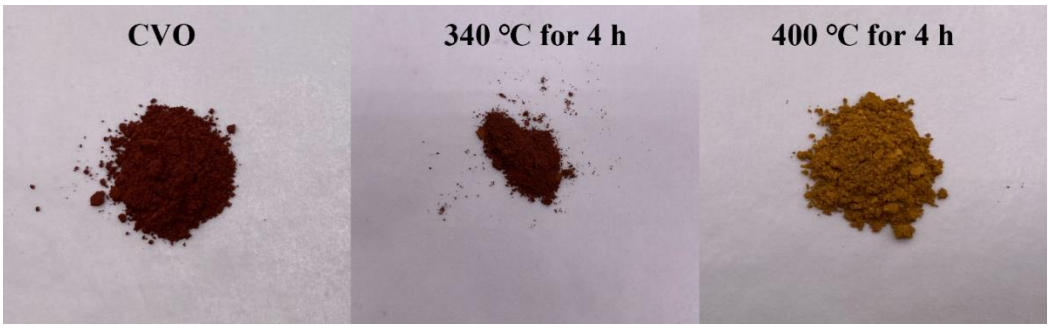

Figure S12. Digital photograph of samples CVO, CVO-340 and CVO-400.

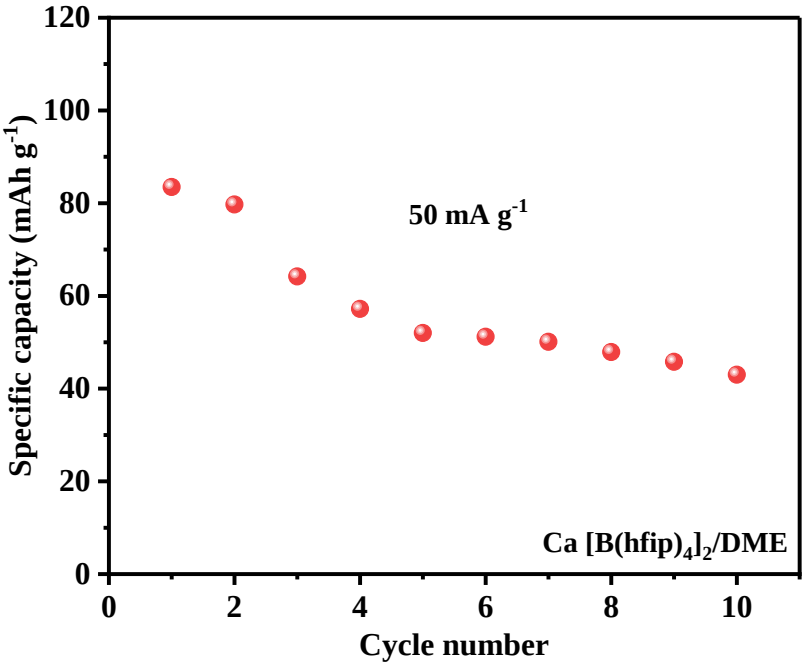

Figure S13. Cycling performance of CVO with $Ca[B(hfip)_4]_2$/DME at 50 mA g^{-1}.

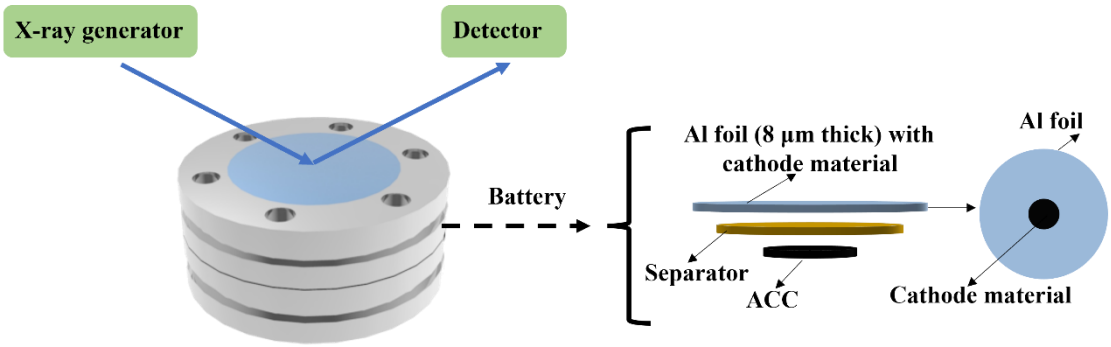

Figure S14. The configuration of the cell for *in-situ* XRD tests.

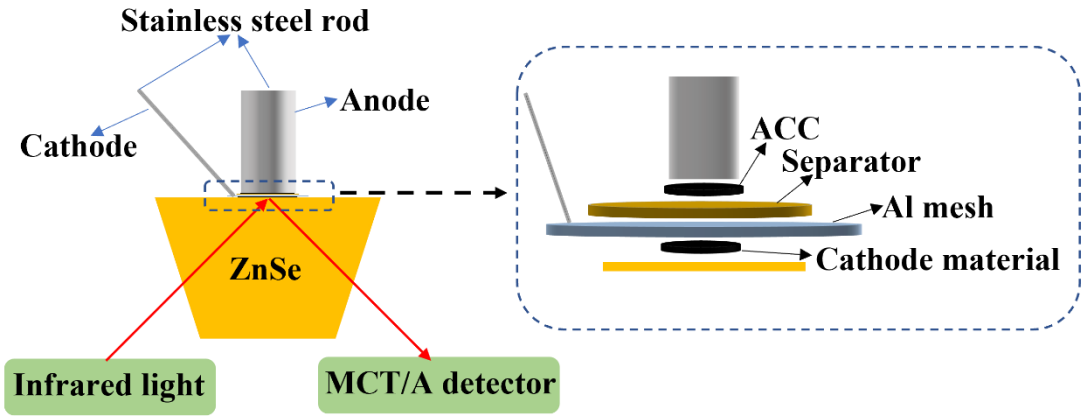

Figure S15. The configuration of the cell for *in-situ* FTIR tests.

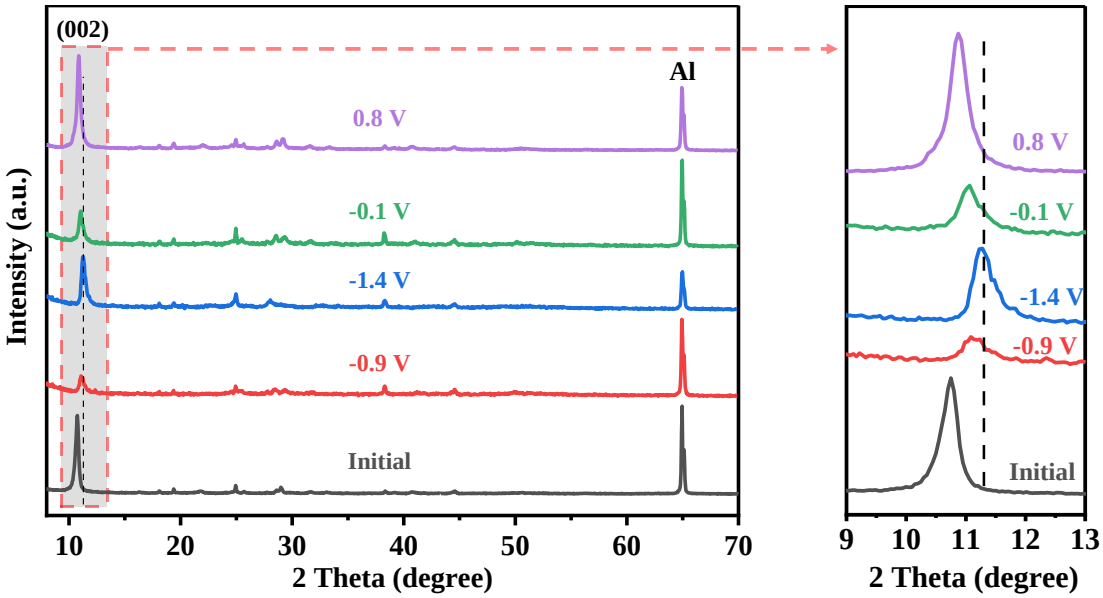

Figure S16. *Ex situ* XRD patterns of CVO at different states.

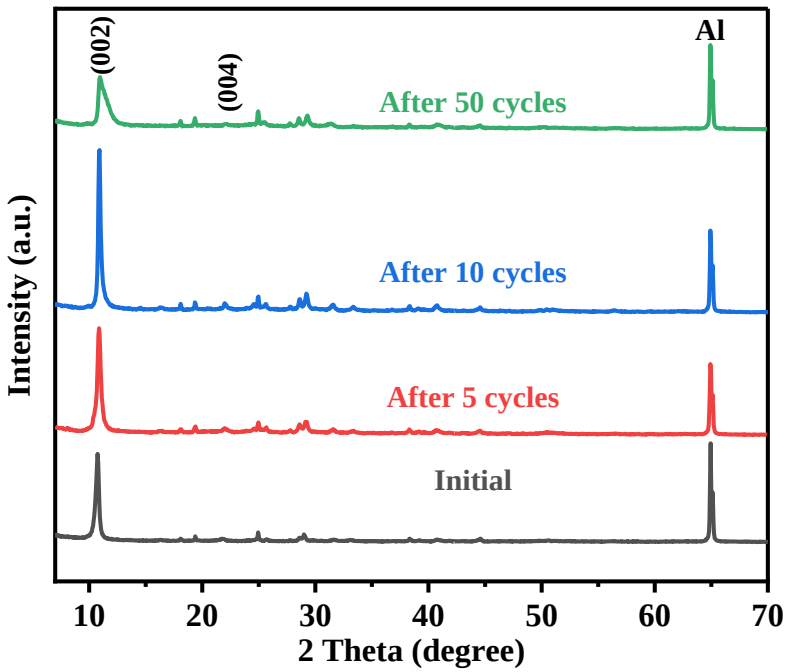

Figure S17. The XRD patterns of CVO after different cycles.

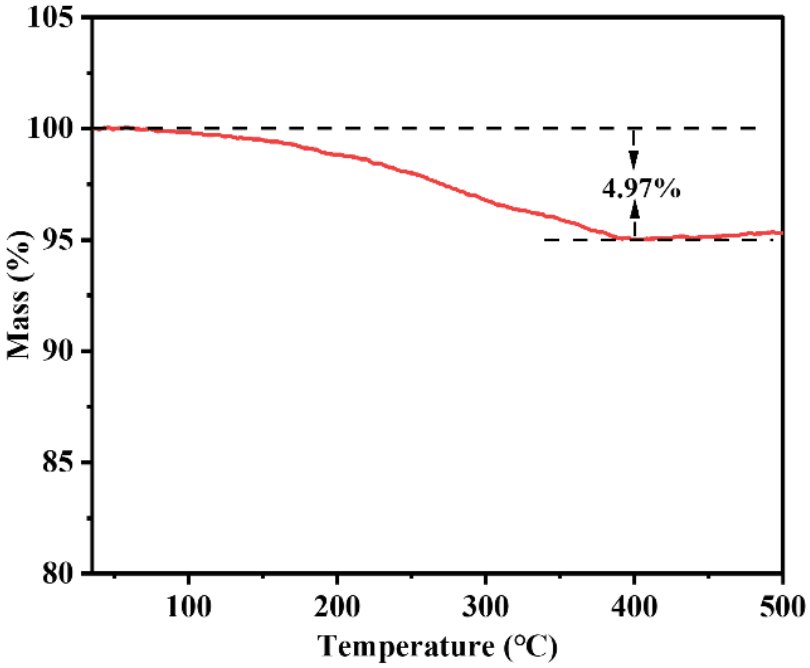

Figure S18. TGA for CVO after 50 cycles.

Z	Element	Family	Atomic Fraction (%)	Atomic Error (%)	Mass Fraction (%)	Mass Error (%)	Fit error (%)
8	O	K	57.66	7.50	30.59	2.63	2.19
20	Ca	K	5.82	1.08	7.73	1.23	2.53
23	V	K	36.52	6.75	61.68	9.69	0.89

Figure S19. The quantitative elemental ratios of CVO at initial state.

Z	Element	Family	Atomic Fraction (%)	Atomic Error (%)	Mass Fraction (%)	Mass Error (%)	Fit error (%)
8	O	K	57.10	6.33	30.99	2.26	1.50
20	Ca	K	13.92	2.40	18.93	2.86	0.43
23	V	K	28.98	5.00	50.08	7.56	0.19

Figure S20. The quantitative elemental ratios of CVO at discharged state.

Table S3. The analysis results of Ca^{2+} insertion sites in CVO.

X Ca^{2+} inserted into CVO (X=0, 1, 2, or 3)	Site	Coordinate (x y z)	Energy (eV)	Volume ($Å^3$)	Volume change (%)
$CaV_6O_{16}·2.8H_2O$	-	-	-936.55	771.42	-
$Ca_2V_6O_{16}·2.8H_2O$	1	(1 0 0.45)	-945.87	788.98	2.28
	2	(0.13 1 0.31)	-944.41	809.35	4.92
	3	(1 0.5 0.5)	-945.92	791.51	2.60
	4	(0.85 1 0.85)	-945.79	781.32	1.28
$Ca_3V_6O_{16}·2.8H_2O$	1+2	-	-951. 54	796.59	3.26
	1+3	-	-953.15	787.33	2.06
	1+4	-	-954.86	791.79	2.64
$Ca_4V_6O_{16}·2.8H_2O$	1+4+2	-	-960.37	803.37	4.14
	1+4+3	-	-961.21	789.85	2.39

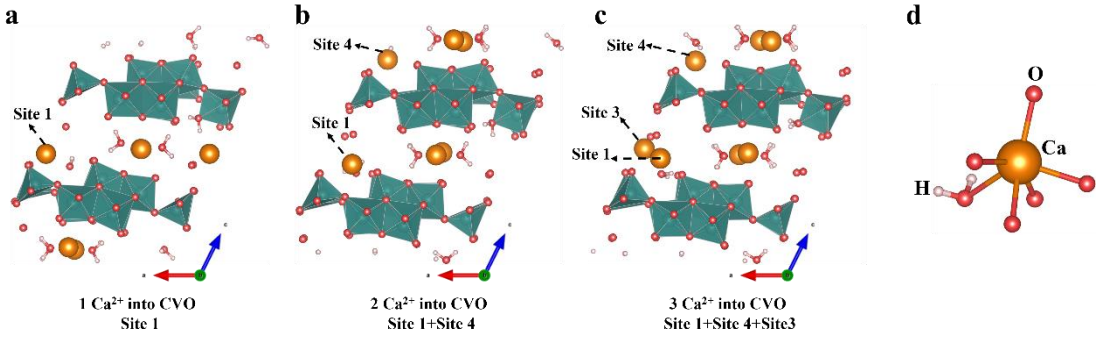

Figure S21. Crystal structure of CVO for (a) one Ca^{2+} inserted into CVO, (b) two Ca^{2+} inserted into CVO and (c) three Ca^{2+} inserted into CVO. (d) The coordination environment of the inserted Ca atom.

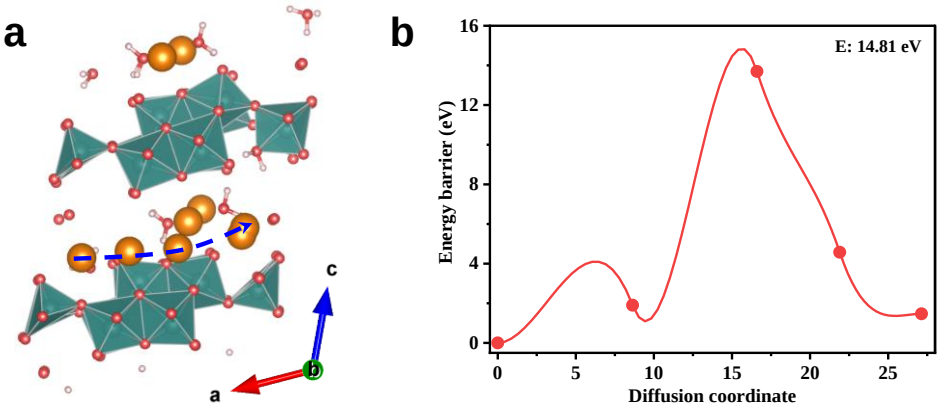

Figure S22. (a) Diffusion path and (b) corresponding diffusion energy barrier profiles of Ca^{2+} along the *a* direction in CVO.

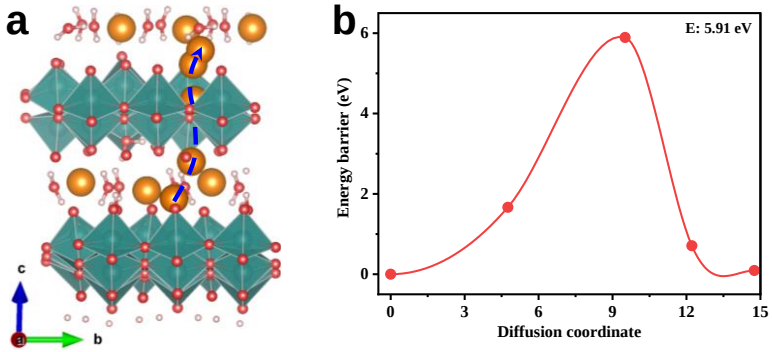

Figure S23. Diffusion path (a) and corresponding diffusion energy barrier (b) profiles of Ca^{2+} along the *c* direction in CVO.

Reference

[1] A. Shyamsunder, L. E. Blanc, A. Assoud and L. F. Nazar, *ACS Energy Lett.* **2019,** 4, 2271.

[2] Z. Li, O. Fuhr, M. Fichtner and Z. Zhao-Karger, *Energy Environ. Sci.* **2019,** 12, 3496.

[3] G. Kresse and D. Joubert, *Phys. Rev. B* **1999,** 59, 1758.

[4] G. Kresse and J. Furthmüller, *Phys. Rev. B* **1996,** 54, 11169.

[5] G. Kresse and J. Furthmüller, *Comput. Mater. Sci.* **1996,** 6, 15.

[6] J. Perdew, K. Burke and M. Ernzerhof, *Phys. Rev. Lett* **1996,** 77, 3865.

[7] M. A. Cooper, F. C. Hawthorne, V. Y. Karpenko, L. A. Pautov and A. A. Agakhanov, *Journal of GEOsciences* **2014**, 159.

[8] X. Zhang, W. Yang, J. Liu, Y. Zhou, S. Feng, S. Yan, Y. Yao, G. Wang, L. Wan, C. Fang and Z. Zou, *Nano Energy* **2016,** 22, 38.

[9] X. Xu, M. Duan, Y. Yue, Q. Li, X. Zhang, L. Wu, P. Wu, B. Song and L. Mai, *ACS Energy Lett.* **2019,** 4, 1328.

[10] A. L. Lipson, B. Pan, S. H. Lapidus, C. Liao, J. T. Vaughey and B. J. Ingram, *Chem. Mater.* **2015,** 27, 8442.

[11] P. Padigi, G. Goncher, D. Evans and R. Solanki, *J. Power Sources* **2015,** 273, 460.

[12] M. Cabello, F. Nacimiento, J. R. González, G. Ortiz, R. Alcántara, P. Lavela, C. Pérez-Vicente and J. L. Tirado, *Elect Electrochem. Commun.* **2016,** 67, 59.

[13] A. L. Lipson, S. Kim, B. Pan, C. Liao, T. T. Fister and B. J. Ingram, *J. Power Sources* **2017,** 369, 133.

[14] T. N. Vo, H. Kim, J. Hur, W. Choi and I. T. Kim, *J. Mater. Chem. A* **2018,** 6, 22645.

[15] M. Cabello, F. Nacimiento, R. Alcántara, P. Lavela, C. Pérez Vicente and J. L. Tirado, *Chem. Mater.* **2018,** 30, 5853.

[16] Y. Murata, S. Takada, T. Obata, T. Tojo, R. Inada and Y. Sakurai, *Electrochim. Acta* **2019,** 294, 210.

[17] N. Kuperman, P. Padigi, G. Goncher, D. Evans, J. Thiebes and R. Solanki, *J. Power Sources* **2017,** 342, 414.

[18] T. Tojo, Y. Sugiura, R. Inada and Y. Sakurai, *Electrochim. Acta* **2016,** 207, 22.

[19] Z. Li, B. P. Vinayan, P. Jankowski, C. Njel, A. Roy, T. Vegge, J. Maibach, J. M. G. Lastra, M. Fichtner and Z. Zhao-Karger, *Angew. Chem., Int. Ed.* **2020**, 59, 11483.

[20] C. Lee, Y.-T. Jeong, P. M. Nogales, H.-Y. Song, Y. Kim, R.-Z. Yin and S.-K. Jeong, *Electrochem. Commun.* **2019,** 98, 115.

[21] W. Ren, F. Xiong, Y. Fan, Y. Xiong and Z. Jian, *ACS Appl. Mater. Interfaces* **2020,** 12, 10471.

[22] Y. Murata, R. Minami, S. Takada, K. Aoyanagi, T. Tojo, R. Inada and Y. Sakurai, AIP Conf. Proc. **2017,** *1807*, 020005.

[23] S. Kim, L. Yin, M. H. Lee, P. Parajuli, L. Blanc, T. T. Fister, H. Park, B. J. Kwon, B. J. Ingram, P. Zapol, R. F. Klie, K. Kang, L. F. Nazar, S. H. Lapidus and J. T. Vaughey, *ACS Energy Lett.* **2020**, 5, 3203.

[24] M. S. Chae, H. H. Kwak and S.-T. Hong, *ACS Appl. Energy Mater.* **2020,** 3, 5107.

[25] J. Wang, S. Tan, F. Xiong, R. Yu, P. Wu, L. Cui and Q. An, *Chem. Commun.* **2020,** 56, 3805.

[26] Z. L. Xu, J. Park, J. Wang, H. Moon, G. Yoon, J. Lim, Y. J. Ko, S. P. Cho, S. Y. Lee and K. Kang, *Nat. Commun.* **2021,** 12, 3369.

[27] M. E. Purbarani, J. Hyoung and S.-T. Hong, *ACS Appl. Energy Mater.* **2021**, 4, 7487.

[28] M. S. Chae, D. Setiawan, H. J. Kim and S.-T. Hong, *Batteries* **2021,** *7*, 54.

[29] J. Hyoung, J. W. Heo, B. Jeon and S.-T. Hong, *J. Mater. Chem. A* **2021**, 9, 20776.

[30] S. J. R. Prabakar, W.-B. Park, J. Y. Seo, S. P. Singh, D. Ahn, K.-S. Sohn and M. Pyo, *Energy Storage Materials* **2021**, 43, 85.